Identification of C-Band Radio Frequency Interferences from Sentinel-1 Data

Andrea Monti-Guarnieri [1,]* **, Davide Giudici** [2] **and Andrea Recchia** [2]

[1] Dipartimento di Elettronica, Informazione e Bioingegneria, Politecnico di Milano, Piazza Leonardo da Vinci 32, 20133 Milan, Italy
[2] ARESYS srl, Via Flumendosa 16, 20132 Milan, Italy; davide.giudici@aresys.it (D.G.); andrea.recchia@aresys.it (A.R.)
* Correspondence: andrea.montiguarnieri@polimi.it; Tel.: +39-02-2399-3446

Abstract: We propose the use of Sentinel-1 Synthetic Aperture Radar (SAR) to provide a continuous and global monitoring of Radio Frequency Interferences (RFI) in C-band. We take advantage of the first 8–10 echo measures at the beginning of each burst, a 50–70 MHz wide bandwidth and a ground beam coverage of ~25 km (azimuth) by 70 km (range). Such observations can be repeated with a frequency better than three days, by considering two satellites and both ascending and descending passes. These measures can be used to qualify the same Sentinel-1 (S1) dataset as well as to monitor the availability and the use of radio frequency spectrum for present and future spaceborne imagers and for policy makers. In the paper we investigate the feasibility and the limits of this approach, and we provide a first Radio Frequency Interference (RFI) map with continental coverage over Europe.

Keywords: SAR; Radio Frequency Interferences; Synthetic Aperture Radar; Geosynchronous SAR

1. Introduction

The availability of radio frequency spectrum is maybe the most critical resource for present and future satellite remote sensing, like microwave passive radiometers or active Earth Exploration Satellite Services (scatterometers, altimeters, wind profilers and SAR [1]). Monitoring the actual spectrum use is currently addressed in L-band [2] and constantly updated using SMOS data [3,4]. An L-band RFI map covering the USA has been made with ALOS data [5,6], while a cube-sat mission for monitoring the whole 6–40 GHz spectrum has been proposed by NASA [7]. In C-band, examples of some RFI monitoring were done by ASCAT scatterometers [8], Envisat and RadarSAT in a dedicated workshop cited in [1], where it was pointed out that the increased exploitation of C-band spectrum for Radio LAN (RLAN) is indeed a major issue for present and future SAR missions.

S1 SAR with its two TOPSAR acquisition modes, the Interferometric Wide Swath (IW) and the Extra Wide Swath (EW), is quite valuable for a frequent and ubiquitous monitoring of C-band RFI for several reasons. The constellation of two satellites [9] is continuously acquiring data over landmasses with a revisit of 1–3 days, thanks to the IW mode wide swath of 250 km with a bandwidth that covers 40–60% of the overall C-band spectrum not open to RLAN (5350–5470 MHz) [1]. Moreover, the burst-mode TOPSAR acquisition, shown in Figure 1 ensures the presence of 8–10 received echoes, in both H and V polarizations, that are unaffected by background scattering, as it will be shown in Section 2, and that can be extracted from S1 raw data. In Section 3 we discuss the method to detect RFI from S1 data, while in Section 4, we show examples of results achieved by processing an entire set of ascending and descending products, covering almost the entire Europe.
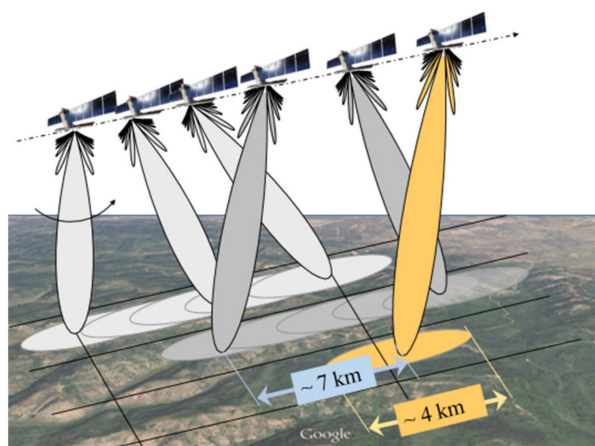
Figure 1. Sketch of TOPSAR acquisition mode, here represented as the three swaths Sentinel-1 IW.

2. Sentinel-1 Acquisition Timeline

We address here Sentinel-1 IW-mode, the default acquisition mode at low and mid latitudes (up to 60°) over still landmasses. At the beginning of each burst, as shown in Figure 1, the antenna beam is pointed backward of −0.6°. During the acquisition it sweeps forward up to +0.6° at the burst end. The system starts acquiring since the transmission of the very first pulse, although no backscatter is foreseen, at least for the two-way sensor-Earth travel-time, which corresponds to 8–10 pulses, that we define "rank" pulses, and are here exploited for RFI monitoring.

The S1 acquisition timeline is made of a fixed pattern of three distinct component. The first part is the preamble, including a number of warmup echoes for instrument stabilization and noise and internal calibration measurements. The central part is the "actual" SAR acquisition and can be several minutes long. For IW mode the adopted timeline is listed in Table 1, the base scheme (duration about 5.4 s) is repeated an integer number of time according to the mission planning. The final part of the data-take is the postamble and includes again internal calibration and noise pulses.

Table 1. IW timeline, cyclically repeated.

Type	Pulse (s)	Rank	PRF (Hz)	Notes
IW1	1409	9	1717.1	
TxCal	12		1717.1	Same pol. of data
TxCal ISO	8		1717.1	H pol
IW2	1548	8	1451.6	
RxCal	20	N/A		No TX
IW3	1410	10	1685.8	
EpdnCal	20	N/A		No TX
IW1	1409	9	1717.1	
TACal	20	N/A		No TX
IW2	1548	8	1451.6	
ApdnCal	20	N/A		No TX
IW3	1410	10	1685.8	
ApdnCal	20	N/A		No TX

The IW data-takes are split into slices of 25 s to ease processing and data dissemination. The slicing procedure is not data driven and the data "cuts" can occur at every time instant within the scheme described in Table 1. At the end of each burst a few calibration pulses are acquired to monitor instrument status during the data-take. Most of the calibration pulses do not foresee any transmission

and hence the "rank" echoes (belonging to IW1 and IW3) acquired after such pulses should contain only noise and RFI coming from the Earth, if any. On the other hand, for the second sub-swath, IW2, the case is slightly different, since the calibration pulses, named "TxCal ISO" in Table 1, are effectively transmitted, but only one cycle over two (as shown in the table) and with antenna beam pointing boresight (approximately 30° with respect to Nadir) and no electronical steering. This means that there could be some potential ground backscatter echo in the first rank pulses of IW2, but only every odd cycle.

The quality of the rank echoes is fundamental for the RFI assessment: we expect that S1 is behaving like a receive-only C-band radiometer. Figure 2 shows the rank echoes power gathered over a very long strip of 730 s, covering from North Africa to arctic. The return power from each of the 20,000 pulses is plotted on the right for both V and H polarizations. It is the superposition of a smooth trend, fast ripples, within 1 dB, and sporadic big spikes, due to RFI. The smooth trend is a good representation of thermal noise, and one can appreciate the sudden changes in the land-sea and see-land transitions, due to the different albedo, like in Crete Island, at 7 s, and the Baltic Sea, at 400 s. A zoom of the ripple pattern has been plotted on the right panel in the same figure: one can observe the saw-tooth behavior with a periodicity of two cycles that matches the timeline listed in Table 1. The shape and the periodicity let then think to transients in the receiver gain after calibration. The ±0.5 dB is well acceptable for sensitive RFI monitoring.
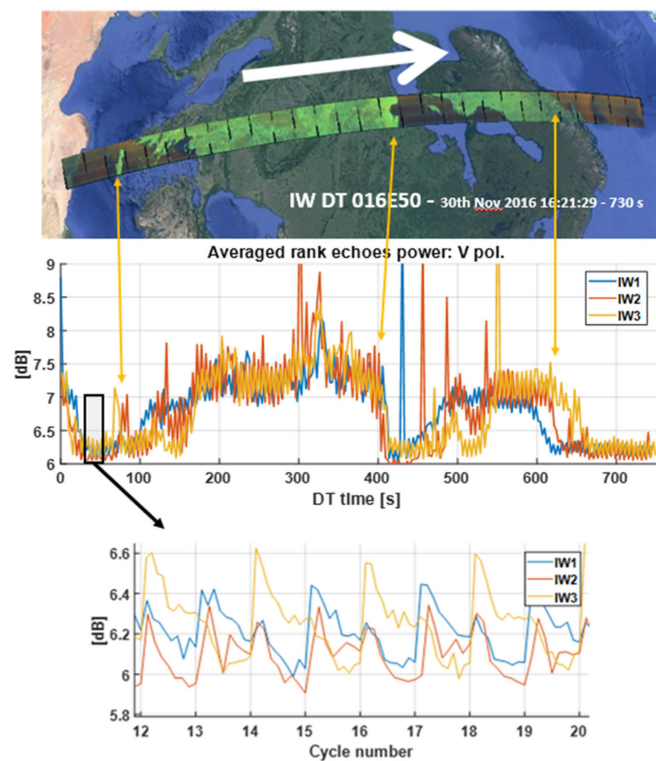

Figure 2. A 730-s long data-take, upper panel, has been used to validate the measure of noise power from rank echoes, mid panel. Notice the changes in the mean power occurring near see/land transitions, as expected from the change in the albedo. A zoom of the power profile, lower panel, shows a saw-tooth behavior with two cycle's periodicity, following the calibration in Table 1.

There is no evidence of a backscatter, not even in the cross-pol echoes in IW2 each two cycles. This result, that comes from the combination of the antenna backward squint (due to TOPSAR), boresight steering, is the key element to enable measures of noise and RFI.

3. RFI Detection and Estimation

The estimation of RFI is carried out according to the method summarized in Figure 3. It comprises a calibration step (on the left in the figure), that runs once in the long term, by exploiting a large amount of data, and an estimation step, on the right, performed on each single data-take.
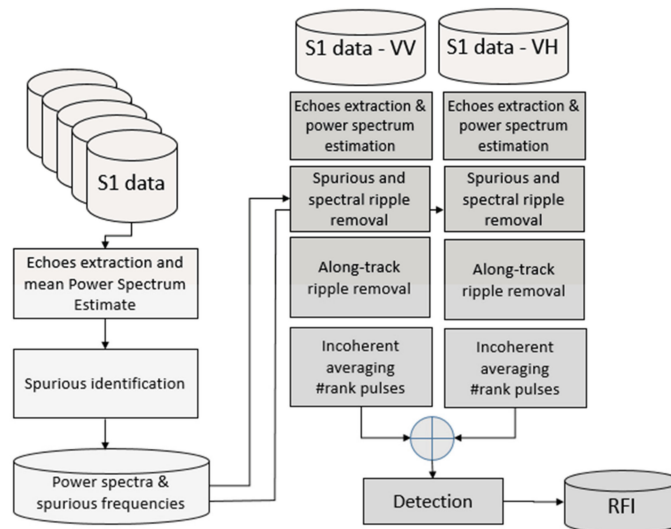

Figure 3. Schematic block diagram for the identification of RFI.

The aim of calibration is the identification of spurious tones and the precise receiver power spectrum profile. In principle, all the combinations of swaths, polarizations, sensors (S1A and S1B) and modes (IW and EW) should be calibrated. In the present study, we focused to IW mode and S1A sensor: the power spectra for the three sub-swaths and the two polarizations are plotted in Figure 4, after averaging over 10,000 bursts in each of the two polarizations, acquired all over the world from November 2016, up to April 2017. S1 demonstrated very good stability in gain, ripples and spurious locations, and this suggest the use of noise data to speed up calibration. A total of 100–200 spectral samples of the whole ~20,000, were found affected by spurious tones, which can be easily detected by a median filter. Once removed, the spectral profiles are estimated and stored.
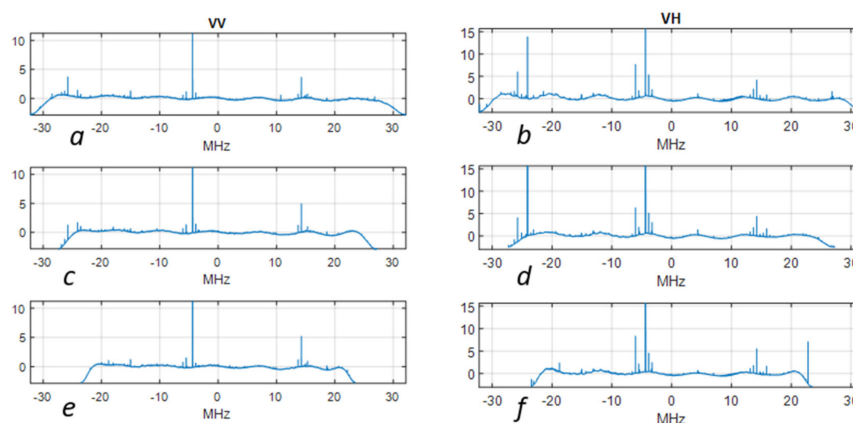

Figure 4. Mean power spectrum density, dB, measured from the "rank" pulses at beginning of each swaths in V (*a,c,e*) and H (*b,d,f*) polarizations, for sub-swaths IW1 (*a,b*), IW2 (*c,d*) and IW3 (*e,f*), averaged on 10,000 bursts. Notice the spurious tones and the ripples.

In the processing step, first the data spectrogram *H(f,t)* is estimated as the squared amplitude of the Fourier Transform of each echo. The frequencies corresponding to the spurious previously identified are nulled. Ripples are then removed in both frequency and time by modelling the expectation of the spectrogram as:

$$E[H(f)] = H_0(f) \times G(t), \tag{1}$$

where $H_0(f)$ is the mean power spectrum estimated by the calibration step, and *G(t)* is the along track ripple pattern, in time domain, as the one shown in Figure 2 on the bottom panel. This second term is not stable in time, as it appears in Figure 2 on the middle panel, and it needs to be estimated from the data. The estimate is carried out by first compensating the range spectra, by the inverse profile $1/H_0(f)$, and then computing the spectral median for each time. The median is robust respect to the RFI that can be in the dataset, however, for further improving RFI rejection, a second order polynomial Savitzky-Golay filter [10] is applied to the along-track profile to derive the estimate of *G(t)*.

An example of a data spectrogram prior and after compensating for the frequency and time-domain ripples is shown in Figure 5. The spectrogram has already been averaged in frequency by a multi-look factor of 100, to reduce noise fluctuation, then enhancing the detection of the slightest RFI.
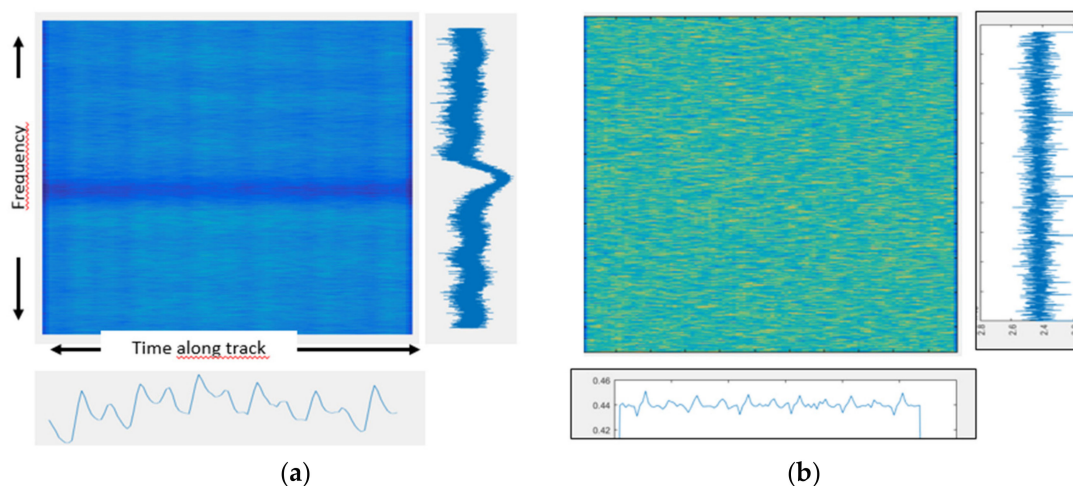

(a)   (b)

Figure 5. Example of a spectrogram of noise data before (**a**) and after (**b**) compensation for the ripples in frequency and time. The residual along-track ripple is less than 0.1 dB.

Detection is performed by a combination of the one tailed Fisher's Z test [6]:

$$Z = \frac{H_f - E\left[H_f\right]}{VAR\left[H_f\right]}, \tag{2}$$

H_f being the power spectrum, and the use Kullback–Leibler (KL) divergence [11], proposed here:

$$K = \int p\left(H_f\right) \log\left(\frac{p\left(H_f\right)}{p_{fit}\left(H_f\right)}\right) dH_f \tag{3}$$

The first detector, (2), finds those extremal peaks, say isolated RFI with powers much stronger than noise one. The KL based detector, in (3), measures the mean distance between the logarithms of the actual power spectrum density distribution, $p(H_f)$, and the Normal one, p_{fit}. This corresponds to the maximum-likelihood hypothesis testing for non-Normal distributed data [12], and is sensitive to maybe many RFI samples of very low power, that is the case of RLAN [13], distributed RFI, or other

factors affecting the raw data quality. An example of identification of low power RFI is shown in Figure 6. The V and H power spectra for the 12 short strips, each formed by the nine rank pulses at the beginning of each burst are shown in a linear scale, normalized with respect to S1 thermal noise floor.
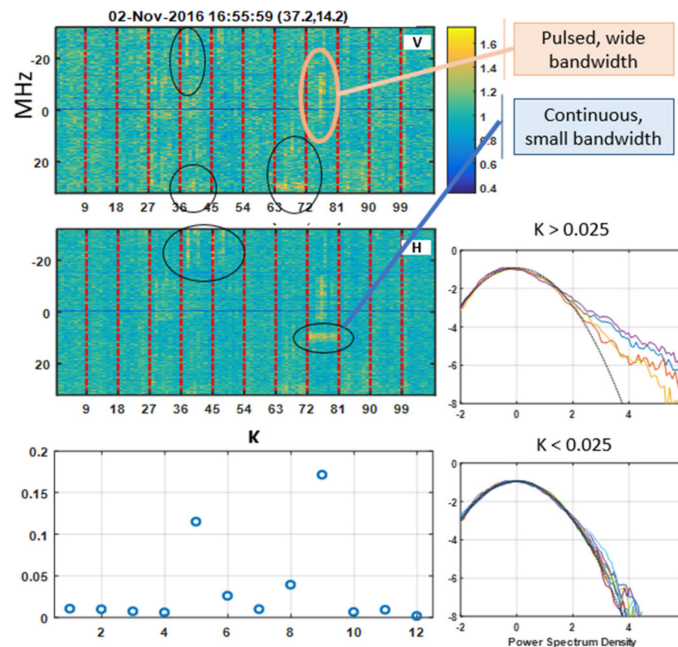

Figure 6. Example of detection of low-power RFI. Top and middle panels on the left: spectrograms for V and H polarizations. Each vertical strip corresponds to the 9 pulses at the beginning of a bursts, all coming from the same sub-swath (IW1). The strongest RFI are encircled. Lower left panel: plot of KL divergence for each burst (*x*-axis define the burst number, and it has been aligned with the spectrograms above). Right panels: histograms, in log scale, and fitting normal PDF, for the bursts with K > 0.025 and K < 0.025.

The multi-looked, whitened spectra are quite homogeneous, and slight deviations may be appreciated, like those encircled. The availability of multiple pulses-per-burst allow to distinguish between pulsed and continuous RFI. As for the detection, the two sets of histograms show that KL divergence was capable to detect those affected by RFI (upper plot) by the others.

4. Sensitivity

The Effective Isotropic Radiated Power (EIRP) of the transmitter causing the RFI contributes to S1 receiver with a power:

$$P_R = \frac{P_{EIRP} \cdot A_S \cdot \eta}{4\pi R^2}, \tag{4}$$

where *As* is the S1 antenna area, η the total losses and *R* the range. The sensitivity is the RFI power that cause the same contribution as noise at S1 receiver:

$$P_n = K_B \cdot T_S \cdot B_{RFI}, \tag{5}$$

K_B being Boltzmann constant, B_{RFI} the RFI bandwidth, T_S is S1 equivalent noise temperature. We can then define the minimal power P_{EIRPZ} of the RFI that gives the same contribution as thermal noise, by equating (4) and (5):

$$P_{EIRPZ} = \frac{K_B \cdot T_S \cdot B_{RFI} \cdot 4\pi R^2}{A_S \cdot \eta}. \tag{6}$$

We can achieve the same result by assuming that S1 is illuminating a homogenous target with backscatter σ_{NESZ} (where NESZ stands for Noise Equivalent Sigma Zero), by a means of a mean power that is the product between S1 peak power and the duty cycle, and contributing to the RFI bandwidth B_{RFI}:

$$P_{EIRPZ} = P_S \cdot dc \cdot \sigma_{NESZ} \cdot \frac{B_{RFI}}{B_S} \tag{7}$$

The evaluation of the sensitivity from (7) is straightforward, given the S1 peak power, $Ps = 5.2$ kW, the duty cycle, $dc = 9\%$, the bandwidth, $Bs = 50$–70 MHz (depending on the swath, see Figure 4) and the σ_{NESZ} as from [14,15]. If we assume S1 requirement $\sigma_{NESZ} < -22$ dB, and a ratio B_{RFI}/Bs of 100 looks over the 20,000 spectral samples in range, we get from (7) $P_{EIRPZ} = 15$ mW for a single tone RFI. This sensitivity becomes as small as 8 mW if the actual figure for S1 $\sigma_{NESZ} = -25$ dB is assumed [14,15]. In that case, the equivalent noise temperature from (6) and (7):

$$T_s = \frac{P_S \cdot dc \cdot \sigma_{NESZ} \cdot A_S \cdot \eta}{K_B \cdot B_{RF} \cdot 4\pi R^2} \tag{8}$$

results in roughly 800 K, by assuming an equivalent antenna area $A_S = 9.6$ m^2, total losses $\eta = -4.5$ dB and $R = 840$ km [14,15].

The sensitivity here computed refers to a single tone RFI, and does not allow to detect such slight RFI in the raw data in time domain. However, for the strongest RFI power exceeds by far that value, say over a factor $20{,}000/100 = 20$, a time domain identification is possible, like the case shown in Figure 7, that refers to the strongest RFI found. The peak power spectrum is 32 dB above the thermal noise level, and the bandwidth is about 5 MHz, that, from (7) evaluated for IW3, gives $P_{EIRP} = 250$ W. Such a high power is still in the dynamic range of S1, from the level of -3 dB to $\sigma_{NESZ}+39$ dB, say with 10 dB margin.
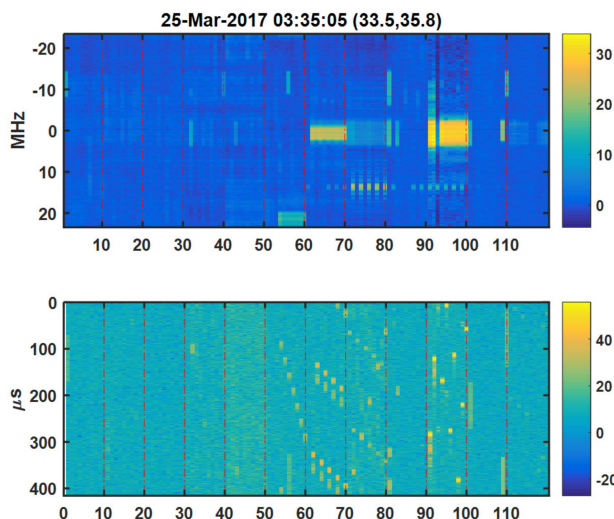

Figure 7. Example of high-power RFI in the spectrogram (**top**); and in the time-along track domain (**bottom**). Color scales are in dB. Horizontal axis is in number of rank pulses that is 10 for IW3.

The method here proposed has been used for estimating RFI all over Europe, in different times—by exploiting ascending and descending passes, and different periods: from November to December 2016 and from February to March 2017. A total of 960 products were considered, spanning 32,000 bursts. In the analysis, we aimed to a very high sensitivity, therefore we discarded the first one-two pulses at the beginning of each burst, since there were still affected by some residual ripples, as shown in Figure 5.

In order to compare the two detectors, we have implemented the Z test in (2) with a very conservative *threshold of 4σ*, which was tuned to the data to exclude false alarms, then we integrated the probability of tails exceeding the threshold:

$$Z = \int_{\mu+4\sigma}^{\infty} p\left(H_f\right) dH_f \tag{9}$$

A comparison between the factor Z and the KL divergence, K, is provided in the bidimensional histogram in Figure 8a, whereas the two values sorted for all the bursts are shown in Figure 8b. In both cases it is possible to notice a two-class behavior, where the thresholds separating the data most likely to be RFI from the good one have been found experimentally from the marginal PDF, plotted on the right, as $\log_{10}(Z_{th}) = -3$ and $\log_{10}(K_{th}) = -1.6$.
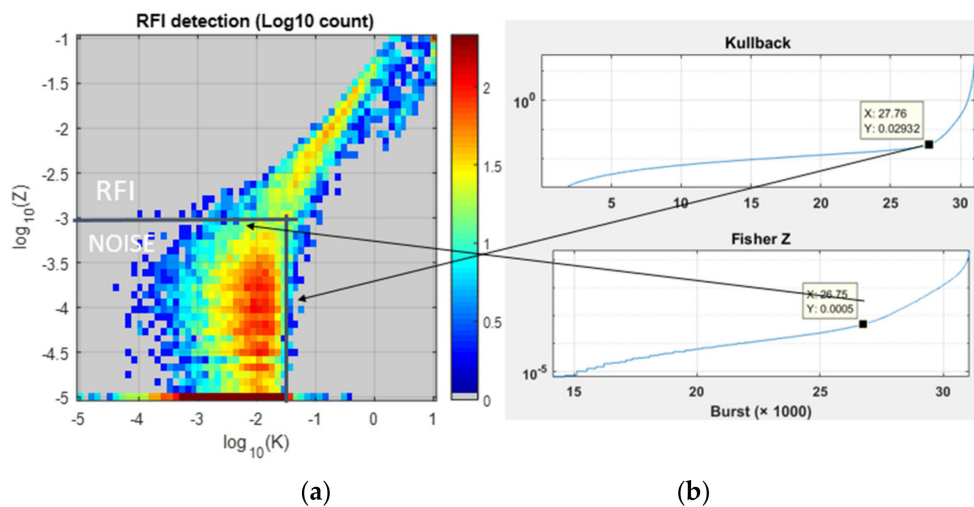

(a)   (b)

Figure 8. (**a**) Bidimensional histogram, counting the power spectra as function of Kullback-Leibler divergence (K), horizontal, and Fisher figure of merit, (Z), vertical, both in log scale. The two classes, marked as noise and RFI, can be separated better in the 2D than by a single figure of merit, either Z, or K; (**b**) Marginal histograms representing the RFI pdf with respect to Fisher and KL divergence.

In order to appreciate the complementarity between Z and K test, we have plotted a set of histograms exceeding the threshold for K, but not for Z (Figure 9a), and vice versa (Figure 9b). In the total of 32,000 bursts, 3800 were classified RFI according to K, then 12% and 4300 according to Z, 14%, whereas the union of K and Z classified 17% of the bursts.
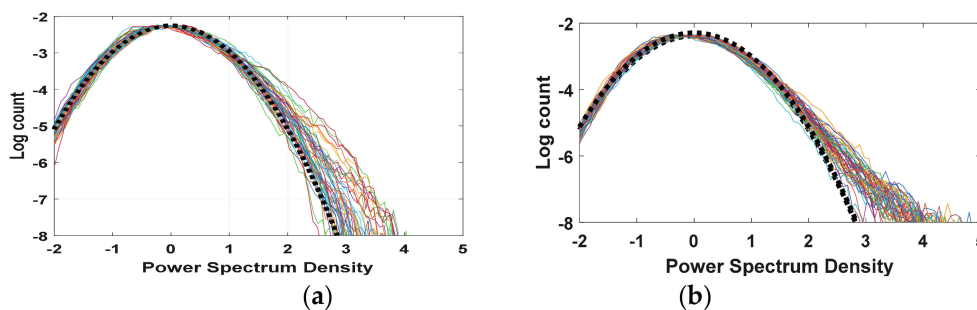

(a)   (b)

Figure 9. Example of histograms where RFI can be identified only by KL divergence (**a**); and of RFI that can be identified by Fisher Z test (**b**).

This confirm the quality of Z test, however, suggests the use of both (at practically the same cost) if searching for very small RFI, like to RLAN [13].

A map of RFI power has been computed by averaging over the rank echoes and over successive passes, both ascending and descending. The map, shown in Figure 10, reports the highest values measured in the whole spectrum. Detection has been made by assuming a very low threshold in order to visualize the slightest RFI, which would include many false alarms. However, one can appreciate that there is a nearly homogeneous background floor below 0 dBm. The power seems loosely correlated with urban areas, therefore not due to RLAN, whereas there are few occurrences co-located with Radar installations, placed as pinpoints in the map, from those listed in [16].
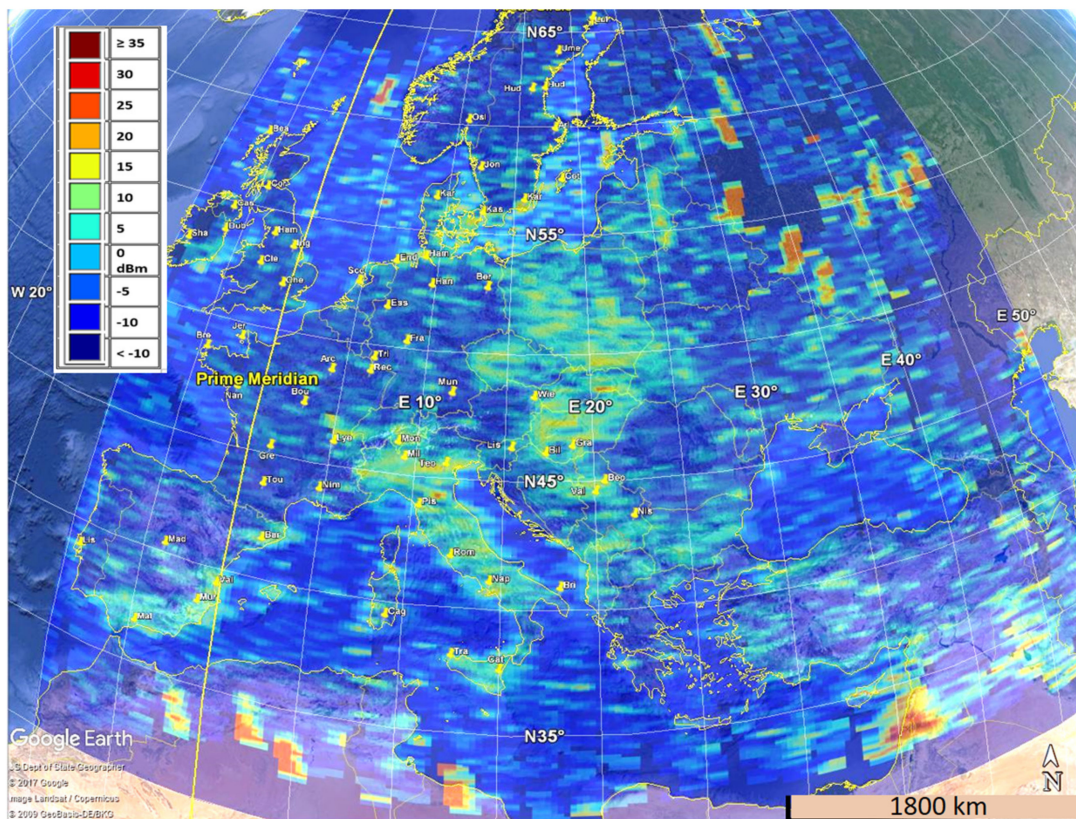

Figure 10. Map of RFI power, averaged in approximately 6 ms. The label superposed marks a part of weather Radar listed in [16].

That power map does not reproduce the spectral occurrence of the RFI. Therefore, we represented in Figure 11, the cumulated histograms of detected RFI power, normalized with respect to S1 noise power, for each frequency bin. The histograms have been normalized so that the figure shows, for each frequency bin, the probability that a certain power level is exceeded. One can notice that, in the majority of the cases, when they are present, the RFI contribute as an additional noise factor less than a figure five, that corresponds to an equivalent temperature of ~4000 K.
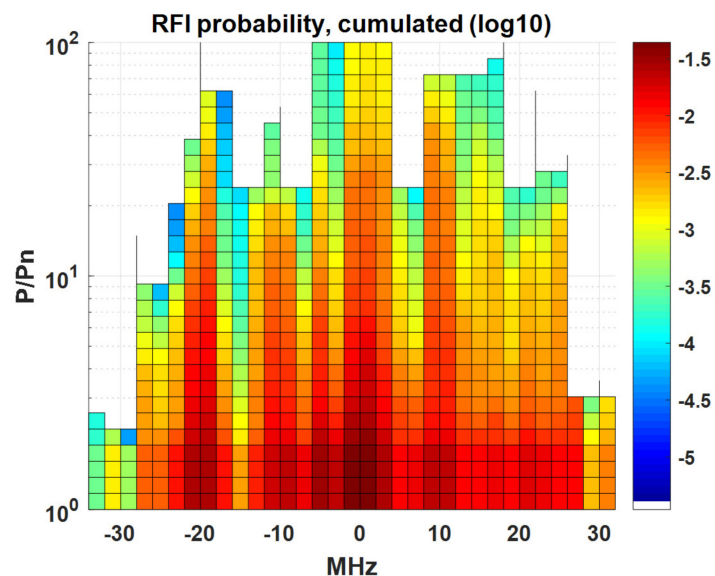
Figure 11. Cumulated histograms of RFI power distributions with frequency, normalized to S1 noise power, estimated by processing data from all-Europe. Vertical scale is probability in $\log_{10}$.

5. Discussion

The main innovation of the proposed method is both in the use of rank-pulses S1 data and in the joint exploitation of two different detectors: Fisher Z test, for the strongest RFI, and KL divergence, sensitive to diffused RFI with low power, like RLAN, that are becoming more and more diffused. The along track squinting of the antenna beam, is a necessary requirement, since it provides rejection to previous transmitted pulses by exploiting the 2D antenna pattern. The method is insofar limited to TOPSAR, and then to S1 (the sole system presently using that mode). Furthermore, the measure is not spanning the whole C-band spectrum, but only up to 40% (in IW1), and it leaves gaps along track, since each swath is sampled for 4 km each 25 km, though near swaths will still be influenced by RFI.

The analysis assumed IW mode data, that exclude RFI detection over polar regions, that are systematically imaged EW mode. Indeed, it could be extended to the EW mode, but the bandwidth would be quite limited, to <20 MHz.

The detection of RFI, carried out with 4σ threshold, would ensure ideally a false alarm rate in the order of $\sim 10^{-5}$. However, this applies with respect to thermal noise, whereas the analysis of rank pulses it has shown time-varying behavior due to internal instrument instability. It is expected that detections above threshold are not to be attributed just to RFI, but also to some internal spurious or transients. Nonetheless, the geo-political correlation of the RFI power maps let think that values starting from RFI of 5 dBm are more likely to be attributed to on-ground sources than to the instrument. This seems to be a reliable sensitivity of the system.

6. Conclusions

The paper proposed the use of the first "rank" pulses per burst to derive a very sensitive RFI monitoring from Sentionel-1 SAR. In fact that, thanks to TOPSAR varying squint, those pulses are ideally unaffected by clutter. This has been demonstrated by a careful analysis of S1 acquisition scheme, and checked by processing hundreds of scenes. The achievement of a high sensitivity, in the order of 8 mW of minimal detectable ground power, requires a careful calibration to remove ripples and spurious tones, and frequency domain multi-looking to suppress random fluctuation of noise power.

Detection of RFI has been then approached by exploiting both Fisher Z test, for the strongest RFI, and Kullback-Leibler divergence, sensitive to diffused RFI with low power, like RLAN. The best results have been found by jointly exploiting the two figures of merit.

The power estimation has been applied to a repeat coverage of Europe comprising ascending and descending passes for a total of 32,000 bursts (each of ~20 km along track and 100 km across track), and producing the first map of C-band RFI power. The analysis evidenced many low power sources, spread over the whole bandwidth, and just a few very high power ones, that are active for only part of the time, and on very precise frequency bands.

The force of this approach is the ubiquitous time and space coverage of S1 constellation, which would ensure the capability of producing and updating a world-wide RFI map.

This map could be exploited by policy makers to understand how important is the RFI issues, and to drive the evolution of the RLAN regulation for WIFI.

The production of these map could be done at a negligible computational cost, and in very short time, if rank pulses are made available apart form the whole raw-datasets (that are totally useless for such goal). This upgrade in S1 products is expected for early 2018.

Author Contributions: Andrea Monti-Guarnieri designed and tested the algorithms and wrote the paper. Davide Giudici had the original idea to exploit the rank-burst, revised the paper, and provided information on Sentinel-1 performance. Andrea Recchia wrote the Matlab code to extract rank pulses from Sentinel-1 raw data, the table and schemes of Sentinel-1 calibration, and made the long strip analyses in Figure 2.

Conflicts of Interest: The authors declare no conflict of interest.

References

1. Ulaby, F.; Lang, D.A. Committee on a Survey of the Active Sensing—Uses of the Radio Spectrum Board on Physics and Astronomy. In *A Strategy for Active Remote Sensing Amid Increased Demand for Radio Spectrum*; The National Academy Press: Washington, DC, USA, 2015; ISBN 978-0-309-37305-0.
2. Soldo, Y.; Cabot, F.; Khazaal, A.; Miernecki, M.; Slominska, E.; Fieuzal, R.; Kerr, Y.H. Localization of RFI sources for the SMOS mission: A means for assessing SMOS pointing performances. *IEEE J. Sel. Top. Appl. Earth Obs. Remote Sens.* **2015**, *8*, 617–627. [CrossRef]
3. RFI Monitoring. SMOS Blog at CESBIO. Web Resource. Available online: http://www.cesbio.ups-tlse.fr/SMOS_blog/?page_id=4087 (accessed on 16 September 2017).
4. Soldo, Y.; de Matthaeis, P.; le Vine, D.; Richaume, P. Comparison of L-band RFI from SMOS and Aquarius observations. In Proceedings of the 2nd SMOS Science Conference, ESA-ESAC, Villafranca, Madrid, 25–29 May 2015.
5. Meyer, F.J.; Nicoll, J.; Doulgeris, A.P. Characterization and correction of residual RFI signatures in operationally processed ALOS PALSAR imagery. In Proceedings of the EUSAR 2012: 9th European Conference on Synthetic Aperture Radar, Nuremberg, Germany, 23–26 April 2012; pp. 83–86.
6. Meyer, F.J.; Nicoll, J.B.; Doulgeris, A.P. Correction and Characterization of Radio Frequency Interference Signatures in L-Band Synthetic Aperture Radar Data. *IEEE Trans. Geosci. Remote Sens.* **2013**, *51*, 4961–4972. [CrossRef]
7. Johnson, J.T.; Chen, C.C.; O'Brien, A.; Smith, G.E.; McKelvey, C.; Andrews, M.; Ball, C.; Misra, S.; Brown, S.; Kocz, J.; et al. The CubeSat Radiometer Radio Frequency Interference Technology Validation (CubeRRT) mission. In Proceedings of the 2016 IEEE International Geoscience and Remote Sensing Symposium (IGARSS), Beijing, China, 10–15 July 2016; pp. 299–301.
8. Ticconi, F.; Anderson, C.; Saldana, J.F.; Wilson, J. Analysis of the noise scenario measured by ASCAT. In Proceedings of the 2015 IEEE International Geoscience and Remote Sensing Symposium (IGARSS), Milan, Italy, 26–31 July 2015; pp. 4882–4885.
9. Potin, P.; Rosich, B. Sentinel-1 Mission Status. In Proceedings of the EUSAR 2016: 11th European Conference on Synthetic Aperture Radar, Hamburg, Germany, 5 October 2016; pp. 1–6.
10. Orfanidis, S.J. *Introduction to Signal Processing*; Prentice-Hall: Englewood Cliffs, NJ, USA, 1996.
11. Kullback, S.; Leibler, R.A. On information and sufficiency. *Ann. Math. Stat.* **1951**, *22*, 79–86. [CrossRef]
12. Gray, R.M. *Source Coding Theory*; Kluwer: Boston, MA, USA, 1990.

13. Scott, P.J.; Sydor, J.; Brandão, A.; Yongacoglu, A. Radio Local Area Network (RLAN) and C-Band Weather Radar Interference Studies. In Proceedings of the 32nd AMS Radar Conference on Radar Meteorology, Albuquerque, NM, USA, 24–29 October 2005.

14. European Space Agency (ESA). *Sentinel-1: ESA's Radar Observatory Mission for GMES Operational Services*; ESA SP-1322/1; ESA Communications: Noordwijk, The Netherlands, March 2012.

15. Collecte Localisation Satellites (CLS). *Sentinel-1A and -1B Annual Performance Report 2016*; doc. MPC-0366, DI-MPC-APR, v1.1; European Space Agency (ESA): Paris, France, April 2017.

16. Newsome, D.H. *Weather Radar Networking: COST 73 Project/Final Report*; Springer: Berlin, Germany, October 2013.